ChemPubSoc Europe

DOI: 10.1002/slct.201803340

Chemistry SELECT Full Papers

Materials Science inc. Nanomaterials & Polymers

Hybrid Films of $Ni(OH)_2$ Nanowall Networks on Reduced Graphene Oxide Prepared at a Liquid/Liquid Interface for Oxygen Evolution and Supercapacitor Applications

Kommula Bramhaiah[+],[a] Chandraraj Alex[+],[a] Vidya N. Singh,[b] and Neena S. John*[a]

Free-standing films of reduced graphene oxide (rGO) based Ni $(OH)_2$ nanowall structures are generated at a liquid/liquid interface involving *in situ* reaction and self-assembly. The nanowall network of $Ni(OH)_2$ sheets anchored on rGO layers with 10–15 nm wall thickness and ordered voids of average size 100 nm can serve as excellent candidates for catalyzing electrochemical oxygen evolution reaction (OER) as they expose maximum edge sites of $Ni(OH)_2$ and allow diffusion and penetration of electrolytes into voids enhancing the contact area of the electrolyte/electrocatalyst interface. The unique morphology of the hybrid films exhibited high electrochemical surface area and low charge transfer resistance. Accordingly, rGO–$Ni(OH)_2$ hybrid films display excellent catalytic activity and high cycling stability in alkaline solutions giving a current density of 10 $mA\,cm^{-2}$ at an overpotential of 378 mV with a Tafel slope of 56 $mV\,dec^{-1}$. The hybrid films also exhibited a high specific and areal capacitance of 1402 Fg^{-1} and 98.12 $mF\,cm^{-2}$ at a scan rate of 5 mVs^{-1}. OER activity and capacitance of the hybrid rGO–$Ni(OH)_2$ films are higher compared to that of bare $Ni(OH)_2$ film and is attributed to the synergic effect between the rGO layer and the ordered interconnected nanowall $Ni(OH)_2$ nanostructures. The primary advantage of these hybrid films is that they can be collected on the desired substrate for ready use as electrodes without the use of any external binders.

Introduction

Increasing global energy demand, depletion of natural resources and environmental problems have driven the scientific community towards the development of clean, efficient and renewable sources of energy as well as technologies associated with the energy production and storage.[1–3] Intense research is being carried out to discover environmentally non-threatening, earth-abundant and low-cost materials for energy-related applications. Water splitting is considered as one of the most promising strategies for the production of clean fuels such as hydrogen and oxygen. Electrocatalytic water splitting reaction is composed of two half-cell reactions; oxygen evolution reaction (OER) and hydrogen evolution reaction (HER). Among these, OER being a four-electron process with sluggish kinetics is considered as a bottleneck for the entire water splitting reaction. For better OER process, it is essential to reduce the overpotential and increase the conversion rates.[3,4] The commercially employed noble metal oxides such as RuO_2 and IrO_2 are also not efficient and their high cost and low elemental abundance limit their practical applications.[5] The non-precious metal oxide based catalysts such as transition metal oxides and layered hydroxides with improved OER activity are of great interest.[6,7] For energy storage, supercapacitors are considered attractive due to their ability to store and deliver energy at a relatively high rate with high power density and energy density, long cycling life and stability.[8] Metal oxide based supercapacitors are widely investigated because of possible high capacitance from a combination of electrochemical double layer capacitance due to reversible adsorption/desorption of ions at the electrode/electrolyte interface and pseudocapacitance due to rapid redox reaction of metal ions on the surface and near surface of the electrode materials.[8,9] Thus, the electrochemical performance of the supercapacitors directly relates to the electrode materials. For better rate capability and stability, materials with porous architecture or hollow nanostructures with short diffusion lengths and abundant active sites are desirable.[10,11]

βNi$(OH)_2$ is regarded as one of the most favourable materials for energy-related applications owing to its good catalytic activity and stability against corrosion during electrochemical reactions in alkaline media.[12] In addition, low cost, earth abundance, facile preparation, layered structure and theoretically high specific capacitance add to their value as potential materials.[13] However, poor electronic conductivity, large volumetric expansion and aggregation during elelctrochemcial cycling limit the electron transport affecting the reaction kinetics.[14,15] Henceforth, to address all these problems, one feasible and effective approach is to fabricate novel hybrid nanostructured materials. The growth of electrocatalysts directly on conductive substrates such as graphene nanosheets,

[a] *Dr. K. Bramhaiah,[+] C. Alex,[+] Dr. N. S. John*
Centre for Nano and Soft Matter Sciences, Jalahalli, Bangalore-560013, India
E-mail: jsneena@cens.res.in
[b] *Dr. V. N. Singh*
CSIR- National Physical Laboratory, Dr. K. S. Krishnan Road, New Delhi-110012, India
[+] *The authors K. Bramhaiah and C. Alex contributed equally to this article.*

Supporting information for this article is available on the WWW under https://doi.org/10.1002/slct.201803340

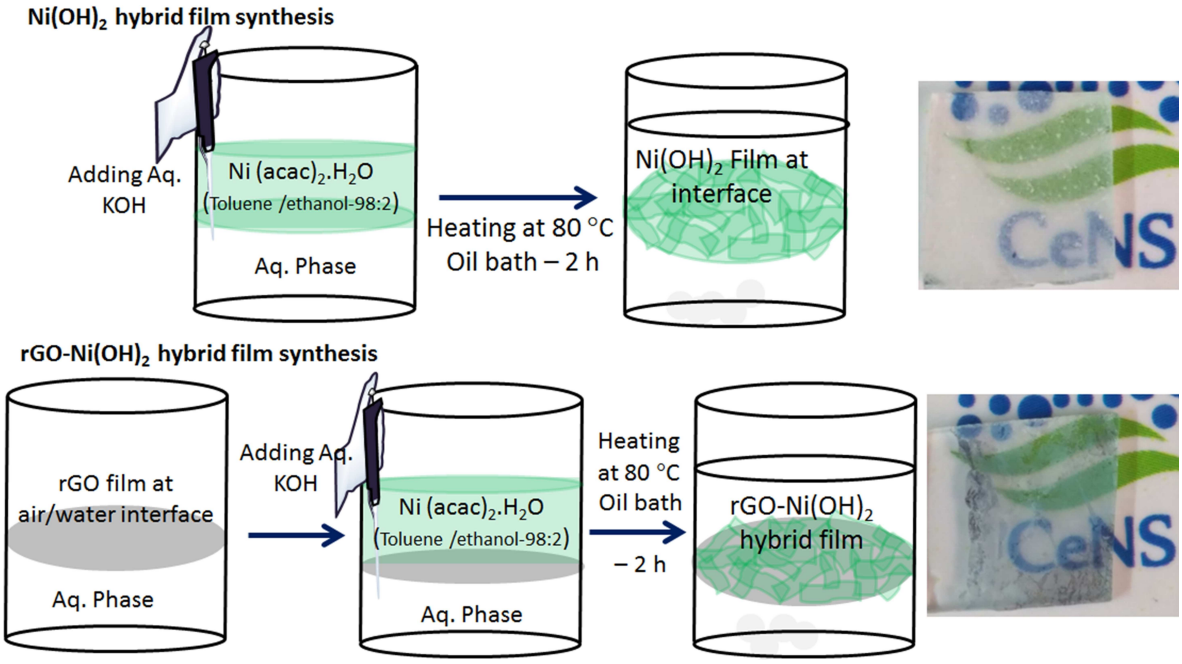

Figure 1. Schematic illustration of the liquid/liquid interface method for the synthesis of $Ni(OH)_2$ and rGO–$Ni(OH)_2$ films and photographs of films transferred on to glass substrates.

carbon nanofibres and nanotubes and Ni foam is an effective way to improve the capacitive performance and cycling stability of the electrode materials by enhancing the electrical conductivity.[15–19] Of particular interest is graphene and its derivatives such as reduced graphene oxide (rGO) possessing high surface area, good mechanical and thermal stability and have been widely investigated for electrochemical applications.[15–17,20–23] Compared to the numerous reports of Ni $(OH)_2$ nanostructures for supercapacitor applications, studies on their oxygen evolution activity are less.[11–17] $Ni(OH)_2$ in the form of nanoparticles, nanosheets supported on Ni foam, nanoplates on multiwalled carbon nanotubes (MWCNTs), nanosheets doped with other active metals on Ni foam, etc have been reported for OER.[18,19,24–27] In a recent report, Zhou et al. has shown that the in-situ growth of β$Ni(OH)_2$ nanoplates on MWCNTs improves OER activity when compared to bare β$Ni(OH)_2$ nanoplates and physical mixture of nanoplates and MWCNTs.[18]

We have sought to develop a facile, low-cost approach for the preparation of ultra-thin, rGO based transition metal hydroxide hybrid films employing a liquid/liquid interface approach. In the past, we have employed the interface method to synthesise a plethora of rGO based metal and metal oxide hybrids for a wide variety of applications in catalysis, surface enhanced Raman spectroscopy, supercapacitors and electrochemical sensing.[28–32] The advantage of the method is that free-standing films over *cm* scale area can be obtained and transferred to any electrode surface. Herein, we present the in-situ growth of vertical $Ni(OH)_2$ nanosheets on rGO at the water/toluene interface. The hybrid material possesses an exquisite morphology with $Ni(OH)_2$ forming a nanowall network over rGO layers. Such arrays of nanostructures and interconnected networks in a vertical fashion are anticipated to serve as good electrode materials for water activation and supercapacitors as they possess distinct advantages over randomly oriented nanostructures.[33] Nanowall network can provide more electrochemical active sites for redox reactions with high exposure of edge sites and enhanced electrolyte penetration due to the highly accessible surface area. In the previous reports, nanowalls of $Ni(OH)_2$ have been prepared on Ni foam employing hydrothermal methods, which is generally time-consuming.[13,34–36] In the present work, thin films of rGO–Ni $(OH)_2$ nanowalls obtained at the liquid/liquid interface are explored for OER activity and supercapacitor application and the performance is compared to that of bare $Ni(OH)_2$ film. The excellent supercapacitance and high OER activity with good cycling stability for rGO–$Ni(OH)_2$ hybrid films as electrode materials are demonstrated.

Results and Discussion

Free-standing, ordered and continuous thin films of nanostructured $Ni(OH)_2$ and rGO–$Ni(OH)_2$ hybrid are obtained employing liquid/liquid interface method. The method involves the alkaline hydrolysis of the metal-organic precursor $Ni(acac)_2$ and self-assembly of $Ni(OH)_2$ nanosheets at the interface to form the films. The reaction and assembly happen on the surface of rGO at the water-toluene interface in the case of hybrid film. The reaction mechanism at the bare and rGO modified interface has been addressed in our previous articles.[28–32] Figure 1 illustrates the preparation of $Ni(OH)_2$ and rGO–$Ni(OH)_2$ nanostructured films employing the liquid/liquid

interface method. The *cm* sale continuous films are transferred to the desired substrates such as glass, fluorine doped SnO_2 glass (FTO), Si or steel substrates for characterisation. The photographs of the films collected on glass substrates (1 cm × 1 cm) are shown in Figure 1. The pale green films appear very thin and translucent. Figure 2 displays the X-ray diffraction

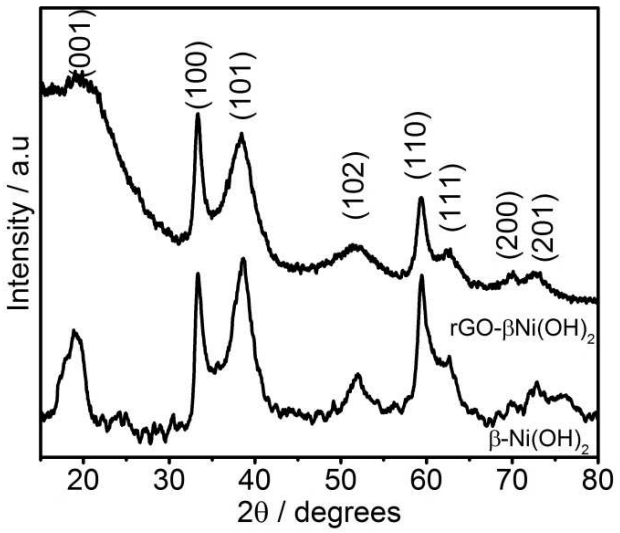

Figure 2. XRD patterns of $Ni(OH)_2$ and rGO–$Ni(OH)_2$ hybrid films prepared at a liquid/liquid interface.

(XRD) patterns of $Ni(OH)_2$ and rGO–$Ni(OH)_2$ hybrid films. The observed peaks at 19.3°, 33.1°, 38.5°, 52.1°, 59.05°, 62.7°, 69.3° and 72.7° correspond to (001), (100), (101), (102), (110), (111), (200) and (201) planes, respectively, of hexagonal β-$Ni(OH)_2$ (PCPDF No. 14–0117).[37,38] The characteristic broad peak of rGO sheets is observed at 23° in the case of rGO–$Ni(OH)_2$ hybrid film wherein (001) plane of $Ni(OH)_2$ is seen superimposed on the rGO peak.

Figure 3a shows the infra red (FT-IR) spectra of $Ni(OH)_2$ and rGO–$Ni(OH)_2$ obtained at the liquid/liquid interface. A narrow and strong band at 3643 cm^{-1} is assigned to the νOH stretching indicating lattice O–H group and inter-sheet H_2O molecules. The intense broad peak present at 3433 cm^{-1} is assigned to the -OH stretching of the free H_2O molecules. Additionally, the bending mode of water molecules is also observed at 1635 cm^{-1}. A strong vibrational band around 514 cm^{-1} corresponds to νNi-OH vibration and that at 469 cm^{-1} corresponds to νNi–O stretching mode.[37–39] These vibrational bands confirm that the as-prepared $Ni(OH)_2$ and rGO–$Ni(OH)_2$ hybrid films are in β (brucite) form.[37] The C=C vibrational band of rGO appears at 1580 cm^{-1}.[30] Raman spectra of bare $Ni(OH)_2$ and rGO–$Ni(OH)_2$ hybrid films are given in Figure 3b. Raman spectra of bare $Ni(OH)_2$ exhibited a strong peak around 3570 cm^{-1} corresponding to the symmetric stretching of the hydroxyl groups (A1g-νOH). A peak around 310 cm^{-1} is assigned to the Eg lattice mode and that at 460 cm^{-1} corresponds to the A1g mode of Ni-OH of Ni-OH.[37,40,41] In the case of rGO–$Ni(OH)_2$, D and G bands due to rGO were observed

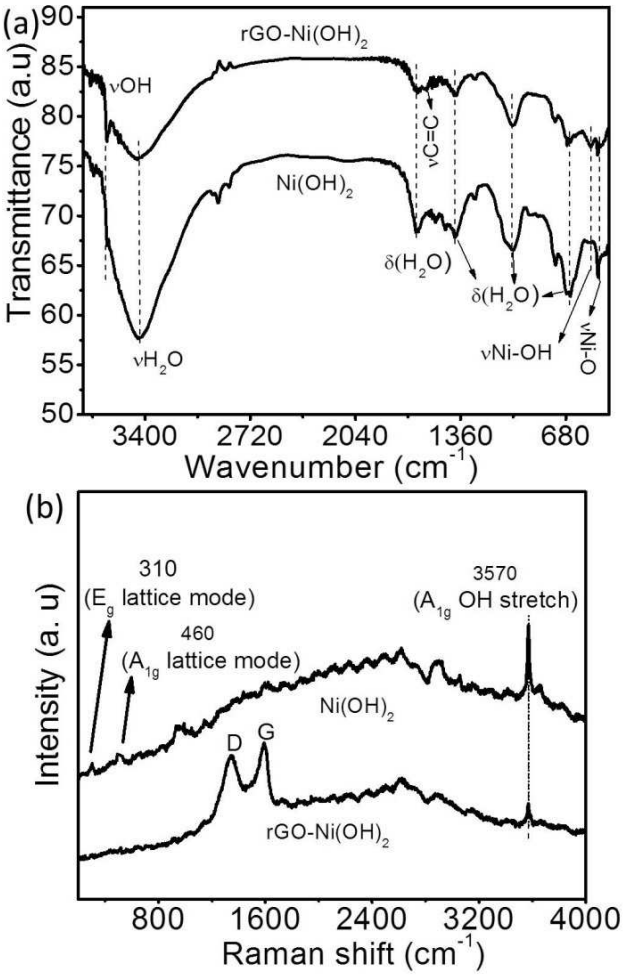

Figure 3. (a) FTIR spectra (b) Raman spectra of $Ni(OH)_2$ and rGO–$Ni(OH)_2$ hybrid films.

at 1346 and 1586 cm^{-1}, respectively in addition to ν(OH) at 3570 cm^{-1}. D band represents the defects in the rGO sheets and G band denotes the in-plane stretching of sp^2 carbon. The intensity profile of D and G band is typical of rGO.[28]

Figures 4a and 4b reveal that $Ni(OH)_2$ films are composed of nanosheets in the vertical fashion, interconnected to form a nanowall network extending to a large area. Figure 4c shows a low magnification image of the hybrid film, rGO–$Ni(OH)_2$, revealing the nanowall network extending to a large area over rGO film. rGO layers can be seen at the edges of the hybrid film. It can be seen that rGO layer surface is homogeneously covered with the $Ni(OH)_2$ nanostructured film. Figure 4d shows high magnification image of rGO–$Ni(OH)_2$ hybrid film and clearly exhibits the highly ordered and nanowall network of Ni $(OH)_2$ on rGO layers. The presence of Ni and O are confirmed by the energy dispersive X-ray spectroscopy (EDS). The average size of the voids formed by $Ni(OH)_2$ nanowall network on rGO layers is around 100 nm and the wall thickness is around ~10-15 nm (Figure S1). The average thicknesses of bare $Ni(OH)_2$ and rGO–$Ni(OH)_2$ films are in the range of ~60 nm (±10 nm) and ~90 nm (±10 nm) and the roughness values are 10 nm and

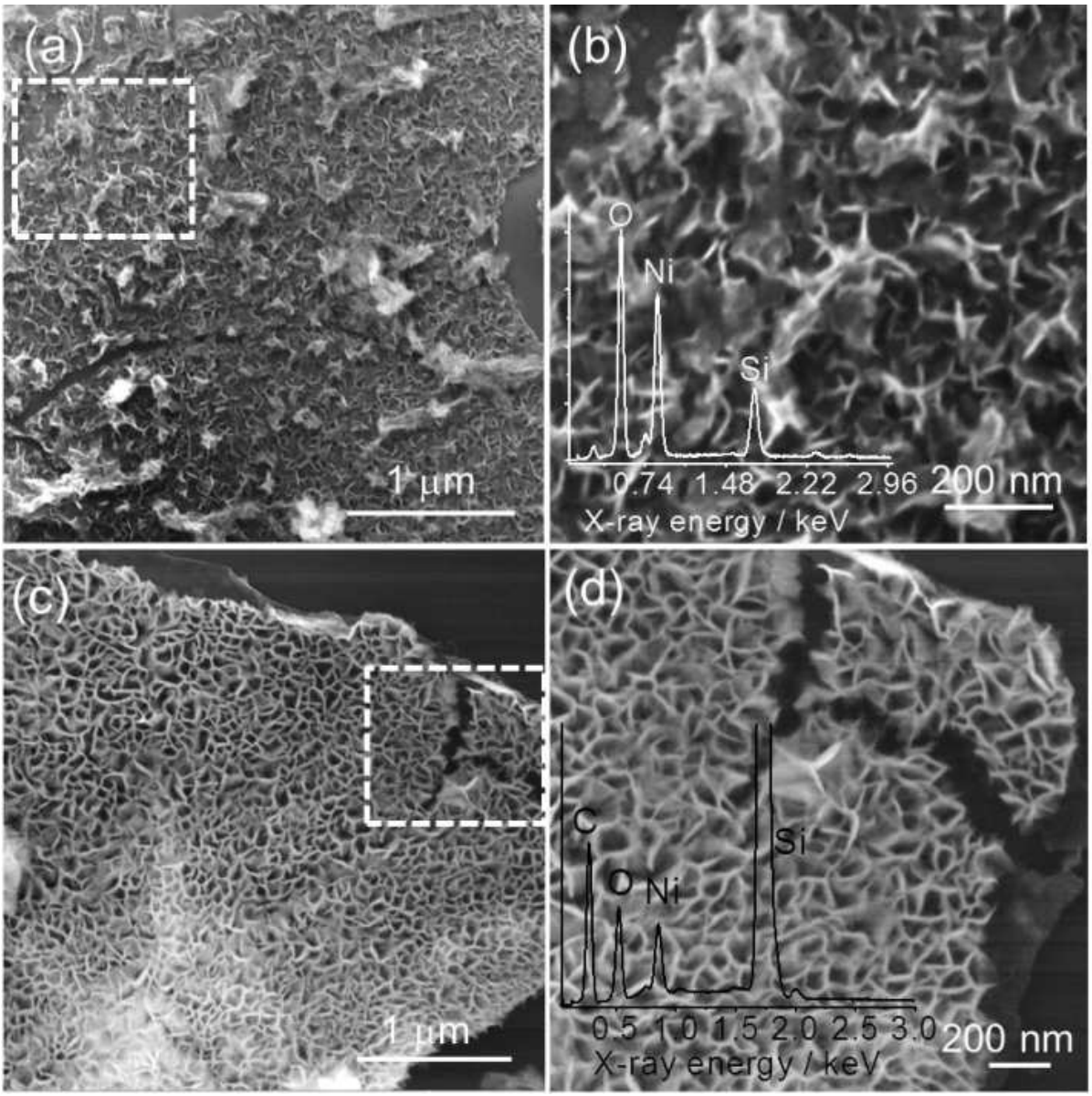

Figure 4. FESEM images (a) bare $Ni(OH)_2$ film (b) magnified image of $Ni(OH)_2$; bottom inset shows the EDS spectra (c) rGO–$Ni(OH)_2$ hybrid film (d) magnified image of the hybrid film; bottom inset shows the EDS spectra.

13 nm, respectively (Table S1, Figure S2). The topography of the hybrid films acquired from atomic force microscopy (AFM) complements the information from field-emission scanning electron microscopy (FESEM) (Figure S3). We have also carried out the elemental mapping using EDS and the details are provided in the supporting information (Figure S4). Transmission electron microscopy (TEM) images further confirm the nanosheet network morphology of $Ni(OH)_2$ and rGO- $Ni(OH)_2$ films (Figure 5). The two-dimensional projection of bare $Ni(OH)_2$ film in TEM shows the nanowall network as a disordered crumpled structure while the hybrid film reveals an ordered structure of nanosheets over rGO (Figures 5a and c). The high-resolution TEM images of $Ni(OH)_2$ given in Figure 5b show the lattice fringes of the nanosheet folds with fringe spacing as 0.46 nm corresponding to *d*(001). Figure 5d shows the high-resolution image of rGO–$Ni(OH)_2$ hybrid film and the inset displays the lattice fringes of *d*-spacing, 0.264 nm and 0.23 nm corresponding to (100) and (101) planes, respectively. Top insets of figures 5b and 5d display electron diffraction patterns from a selected area (SAED) corresponding to (100), (101) and (110) of $Ni(OH)_2$. It is evident from the electron micrographs that the $Ni(OH)_2$ nanowalls are less ordered in the case of bare film with collapse of the sheets in many regions. In contrast, the hybrid films contain a more uniform and highly ordered network of $Ni(OH)_2$ nanowalls on rGO similar to the case of an array indicating that rGO acts as a scaffold in anchoring the Ni $(OH)_2$ sheets, probably by coordinating Ni^{+2} ions from the toluene phase and OH^- from the aqueous phase, simulta-

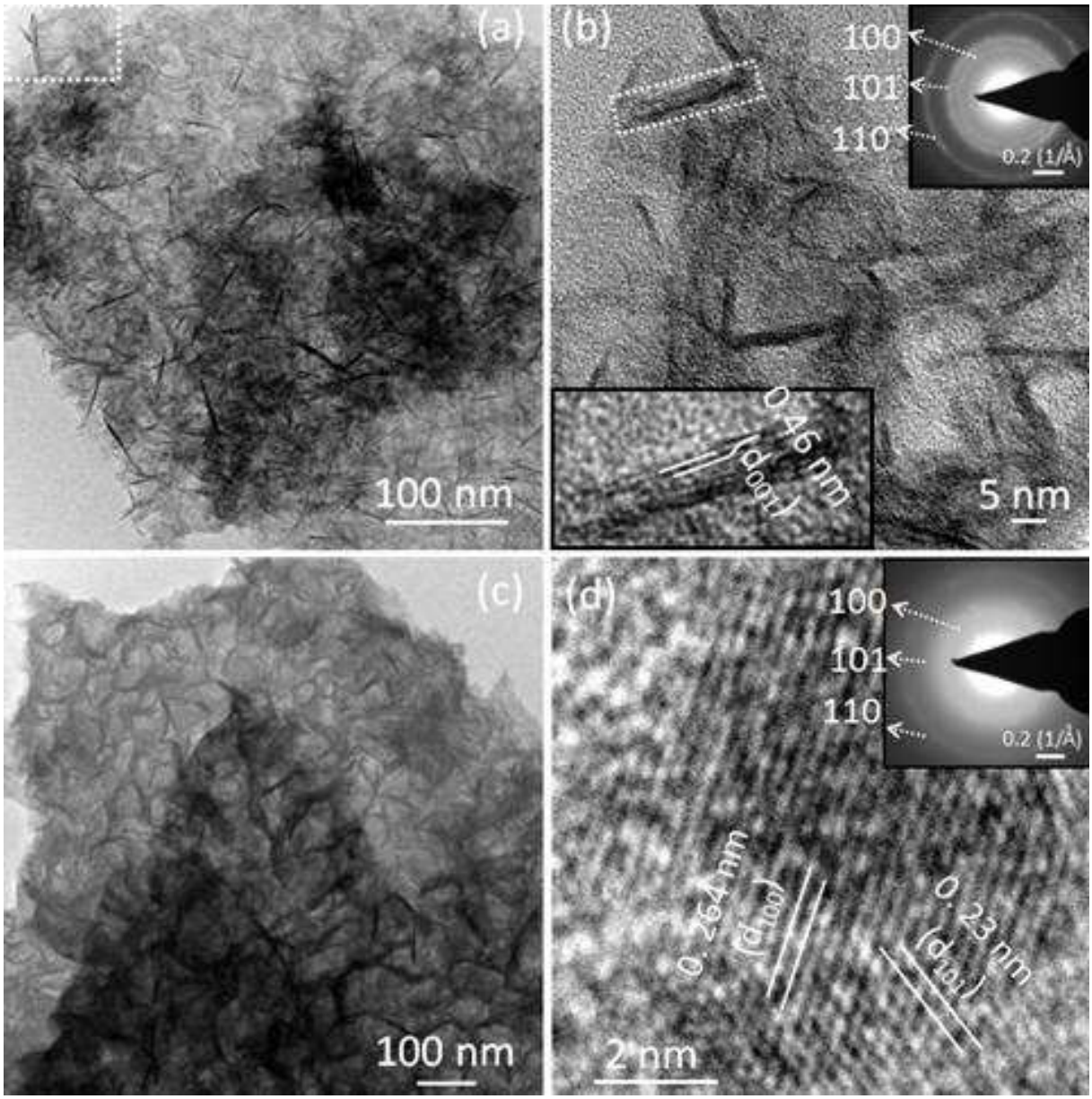

Figure 5. TEM images (a) $Ni(OH)_2$ film (b) high-resolution image of (a); insets show the SAED pattern and high-resolution image (c) rGO–$Ni(OH)_2$ film (d) high-resolution image of (c); inset shows SAED pattern.

neously. Interestingly, the nanowalls are highly interconnected to form ordered voids.

The nanostructure formed due to interconnected nanowalls with nanoscale thickness can contribute to the high specific surface area of the material. The 2D network of the films should permit easy accessibility of ions to the electrode/electrolyte interface and the ordered vertical nanowall network with voids anchored on the rGO surface facilitates the penetration of electrolyte with the maximum accessible area. Hence, we envisage better electrochemical performance of these films prepared at the interface. The large area, free-standing films allow the facile preparation of the electrodes, where in the films are lifted on to the steel substrates directly and employed as working electrodes. The electrocatalytic activity of the rGO–$Ni(OH)_2$ hybrid film towards OER has been investigated and compared with the bare $Ni(OH)_2$. We have also investigated the supercapacitance of these hybrid films.

OER Activity

Figure 6a displays linear sweep voltammetry (LSV) of steel substrate, bare $Ni(OH)_2$ and rGO–$Ni(OH)_2$ hybrid films in 1 M KOH (pH = 14) measured at a scan rate of 5 mVs^{-1}. rGO–$Ni(OH)_2$ hybrid film exhibits an overpotential of 378 mV at a current density of 10 $mA\,cm^{-2}$, while bare $Ni(OH)_2$ film exhibits an overpotential of 421 mV at 10 $mA\,cm^{-2}$. The current density

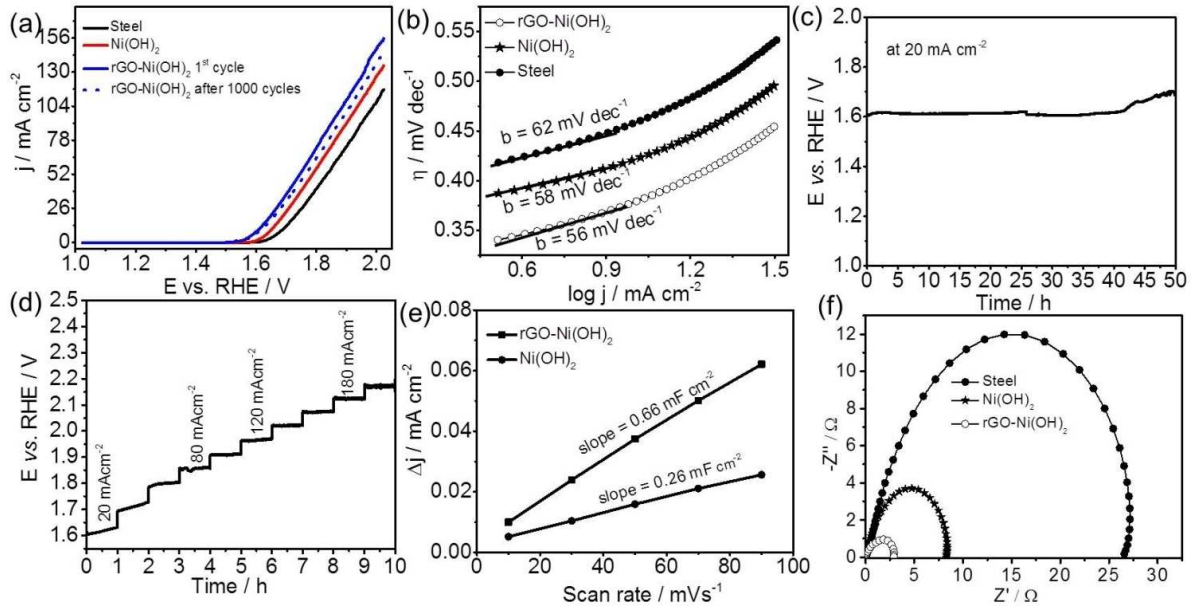

Figure 6. (a) Linear sweep voltammetry of as-synthesised hybrid films coated on steel substrates (b) Tafel plots (c) Chronopotentiometric curve at 20 mA cm^{-2} current density for 50 h (d) Multistep CP curve at varying current densities ranging from 20 −200 mA cm^{-2} with an increment of 20 mA cm^{-2} per 1 h (e) Plots of Δj vs. scan rate (f) Nyquist plots measured at a potential of 1.64 V (vs. RHE).

obtained for the hybrid film is higher than the bare film and both cases exhibit higher current density than the steel substrate. The long-term stability is one of the most important requirements for the determination of the activity of the electrode materials. We have carried out cyclic voltammetry (CV) measurements at a scan rate of 100 mVs^{-1} for 1000 cycles followed by LSV measurements at a scan rate of 5 mVs^{-1} (Figure 6a). The rGO–Ni(OH)$_2$ hybrid film exhibits an overpotential of 389 mV at 10 mA cm^{-2} current density after cycling, which is only slightly higher than the initial value indicating their good stability and cycle performance. Figure 6b shows the Tafel plots that are obtained from the LSV measurements and Tafel slope, *b* is estimated to compare the electrocatalytic activity of the various electrode materials. A lower Tafel slope corresponds to higher OER kinetics. At lower overpotential (< 450 mV), the apparent Tafel slopes are 56 mV dec^{-1} for the hybrid rGO–Ni(OH)$_2$ films, 58 mV dec^{-1} for bare Ni(OH)$_2$ and 62 mV dec^{-1} for steel substrate (Figure 6b). For overpotential >450 mV, the Tafel slopes are 153 mV dec^{-1} (rGO–Ni(OH)$_2$), 164 mV dec^{-1} (bare Ni(OH)$_2$) and 183 mV dec^{-1} (steel substrate) (Figure S5a). It is known that the Tafel slopes and the associated kinetic parameters are potential-dependent and is usually attributed to the changes in the rate determining step. At higher overpotentials, the availability of surface active sites are more for bubble nucleation causing entrapment and shielding of the catalytic activity.[42] It is obvious from LSV and Tafel plots that nickel hydroxide nanosheets exhibit good electrocatalytic activity for the oxidation of water. In alkaline media involving 4-electron transfer pathway for OER, the formation of OOH* intermediate is the rate determining step facilitated by NiOOH formation with an average oxidation state of 3.6 under OER potential.[43–45] The rGO–Ni(OH)$_2$ hybrid films exhibit a stronger redox peak in cyclic voltammogram than bare Ni(OH)$_2$ film (Figure S5b) supporting the presence of more active sites in hybrid film. This is possible as the ordered vertical nanowalls possess more edge sites with Ni^{+2} ions in lesser co-ordination facilitating easy formation of Ni^{+2} to Ni^{+3} ions improving the electrocatalytic activity. Moreover, combining Ni(OH)$_2$ with rGO sheets can significantly decrease the charge transfer resistance supported by the impedance analysis as discussed later. The presence of rGO can also render stability to Ni(OH)$_2$ sheets by suppressing aggregation during cycling. The catalytic activity of the various reported Ni(OH)$_2$ nanostructures and their composites are listed in Table 1. It can be seen that rGO–Ni(OH)$_2$ nanowall films presented in this work exhibits superior OER activity very close to the performance of RuO_2 and IrO_2. The ordered nanowall network structure with exposure of edge sites and large accessible surface area due to voids can aid in achieving the large current response. The enhanced activity of the hybrid film could be attributed to the synergistic effect of rGO and Ni(OH)$_2$, rGO providing improved electrical conductivity along with large surface area and Ni(OH)$_2$ nanowalls providing enhanced active sites and electrolyte penetration. To address the long-term stability of the rGO–Ni(OH)$_2$ hybrid film, we have carried out chronopotentiometry (CP) measurements at a constant current density of 20 mAcm^{-2} (Figure 6c). The potential is stable for up to 40 hr and further, it is seen to increase and may be attributed to the mechanical deformation and swelling of the material by volume change.[46,47] The electrode stability at different applied current densities using multistep CP measurements in the range of 20–200 mAcm^{-2} is given in Figure 6d. Up on increasing the current density, the potential of the rGO–Ni(OH)$_2$ hybrid film also

Table 1. The catalytic activity of the recently reported $Ni(OH)_2$ nanostructures for OER performance

Catalyst composition	Electrolyte	Tafel slope (mV dec^{-1})	η at 10 mA cm^{-2} (mV)	References
rGO–$Ni(OH)_2$ nanowall film	1 M KOH	56	378	***This work***
$Ni(OH)_2$ nanowall film		58	421	
MWCNTs/$Ni(OH)_2$ nanoplates	0.1 M KOH	87	474	18
MWCNTs + $Ni(OH)_2$ nanoplates		140	540	
β$Ni(OH)_2$ nanoplates		165	595	
Electrodeposited $Ni(OH)_2$ film	1 M KOH	106-134	529-605	48
β$Ni(OH)_2$ plates	0.1 M KOH	111	444	49
β$Ni(OH)_2$ nanoparticles		246	–	
α$Ni(OH)_2$ nanocrystals		42	331	
NiO_x nanoparticles/PEI-CNT	1 M NaOH	40	410	50
$Ni(OH)_2$/rGO	1 M KOH	50	356	51
$Ni(OH)_2$/Ag/rGO		32	292	
$Ni(OH)_2$		53	387	
Graphene/NiO(OH)	1 M KOH	173	567	52
Graphene/$NiFe_{0.3}O$(OH)		76	372	
Graphene/$NiFe_{0.56}O$(OH)		67	390	
$Ni(OH)_2$ / Carbon paper	1 M KOH	101.9	308	53
Ni/NiO(OH)/nitrogen doped carbon matrix	0.1 M KOH	40	390	54
NiCo layered double hydroxide / Ni foam	0.1 M KOH	113	420	55
NiCo hydroxide	0.1 M KOH	65	460	56
NiCo layered double hydroxide	1 M KOH	40	367	57
$Ni(OH)_2$/ NiAl foil	1 M KOH	–	289	58
NiCo(OH)x	1 M KOH	109	410	59
RuO_2	1 M NaOH	64.7	430	60
IrO_2		47.7	430	

increased and stabilized rapidly, suggesting that the hybrid film exhibit excellent mass transfer and mechanical stability.[46,47]

Electrochemical surface area (ECSA) is an important parameter directly related to the electrocatalytic activity of the electrode materials. We have estimated the ECSA values for bare $Ni(OH)_2$ and rGO–$Ni(OH)_2$ hybrid from CV plots (Figure S6) and Δj vs. scan rate plot given in Figure 6e employing the expression, $ECSA = C_{dl}/C_s$, where C_{dl} is the double layer capacitance and C_s is the specific capacitance of the flat, standard sample.[61,62] The standard theoretical specific capacitance values are not available for bulk NiO_x and $Ni(OH)_2$ and *Cs* value (25 μF cm^{-2}) for Ni electrode in 1 M NaOH was applied [62]. The calculated ECSA value for rGO–$Ni(OH)_2$ hybrid film is 26.4 cm^2 and bare $Ni(OH)_2$ film is 10.4 cm^2. In the literature, Tian et al. observed an ECSA of 0.037 cm^2 for wafer scale, 1.4 nm ultra-thin $Ni(OH)_2$ nanosheets and also studied the effect of thickness on the ECSA measurements. With the increase in thickness of the film from 1.4 nm to 230 nm, the ECSA values decreased to 0.027 cm^2. The observed ECSA values in the present work are higher than the reported values.[45] It is well known that surface atoms of the electrode material play substantial role in the OER process.[61,62] The higher ECSA values obtained for rGO–$Ni(OH)_2$ nanostructures also support the higher penetration of electrolyte ions towards higher OER activity.

Electrochemical impedance spectroscopy (EIS) is performed to understand the oxygen evolution interfacial reaction and charge transport mechanisms of the electrode materials. Figure 6f displays the typical Nyquist plots of steel substrate, bare $Ni(OH)_2$ and rGO–$Ni(OH)_2$ hybrid film modified electrodes acquired at a constant potential of 1.64 V (vs. RHE) in 1 M KOH electrolyte solution. The calculated R_{ct} values of the steel substrate, bare $Ni(OH)_2$ and rGO–$Ni(OH)_2$ nanostructured hybrid film are 26.5 Ω, 8.3 Ω and 2.8 Ω, respectively. The lower R_{ct} value for the rGO–$Ni(OH)_2$ film electrode indicates better electron transport within the hybrid film and agrees well with the faster OER rates observed in the LSV measurements.

Supercapacitor

The supercapacitor performance of $Ni(OH)_2$ and rGO–$Ni(OH)_2$ hybrid films prepared at a liquid/liquid interface were studied by carrying out CV, galvanostatic charge and discharge (GCD) and EIS measurements of the films on steel substrates in 3 M KOH employing a three electrode electrochemical cell. The CV curves of various films at 50 mVs^{-1} are shown in Figure 7a. The observed pronounced redox peak reveals the pseudocapacitance behaviour of the films. The anodic peak observed around 0.48 V and the cathodic peak around 0.36 V correspond to the electrochemical oxidation of $Ni(OH)_2$ to NiOOH and the reverse reduction process from NiOOH to $Ni(OH)_2$, respectively. The process of oxidation and reduction are given in the following expression, $Ni(OH)_2 + OH^- \leftrightarrow NiOOH + H_2O + e^-$. Based on the CV curves depicted in Figure 7a, it is obvious that the capacitance of rGO–$Ni(OH)_2$ hybrid film is much higher than that of bare $Ni(OH)_2$ film.

The specific (C_s) and areal (C_a) capacitance values of the hybrid films have been calculated from CV curves employing the expression $C = (\int I(V)dV/2mv\triangle V$, where $\int I(V)dV$ is the integrated area of the CV cycle, *m* is the mass of the active material (g) or area of the active material (cm^2) on the electrode surface, *v* is the scan rate (V/s) and $\triangle V$ is the potential window range in the CV measurement.[22,23,29,63] Accordingly, the values obtained at a scan rate of 5 mVs^{-1} are $C_s = 260\ Fg^{-1}$ & $C_a = 18.2\ mF\,cm^{-2}$ for bare $Ni(OH)_2$, and $C_s = 1402\ Fg^{-1}$ & $C_a = 98.12\ mF\,cm^{-2}$ for rGO–$Ni(OH)_2$. A 5 fold higher specific and areal capacitance can be noticed in the case of rGO–$Ni(OH)_2$ hybrid film compared to that of bare $Ni(OH)_2$ film. The higher capacitance is due to the synergic contribution of double layer capacitance from rGO and pseudocapacitance from $Ni(OH)_2$. The large surface area of the rGO films along with a network of nanowall thin sheets of

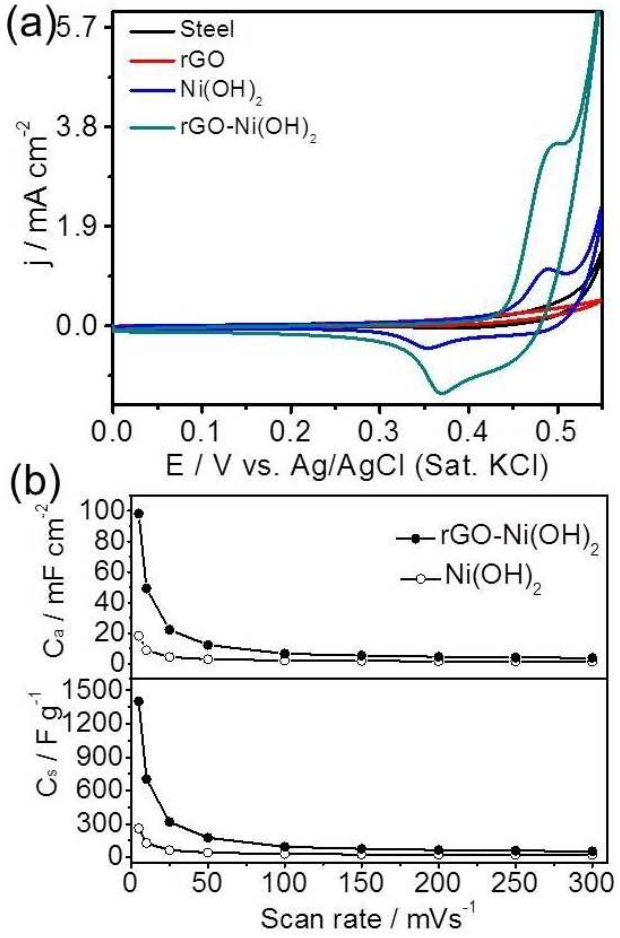

Figure 7. Electrochemical measurements (a) Cyclic voltammetry curves of various modified electrodes; bare steel, rGO, $Ni(OH)_2$ and rGO-β$Ni(OH)_2$ hybrid film at 50 mVs^{-1} (b) Plot of areal and specific capacitance vs. scan rate for various films.

$Ni(OH)_2$ provide a large contact area with the electrolyte solution thereby enhancing the ion adsorption. The rGO film aids the electron transport between the $Ni(OH)_2$ and the electrode. The effect of scan rate on the capacitance of hybrid films has also been studied. The CV response of bare $Ni(OH)_2$ and rGO–$Ni(OH)_2$ hybrid films at different scan rates ranging from 5–300 mVs^{-1} is shown in Figure S7. The plot of scan rate versus peak current (Figure S8) displays the variation of anodic and cathodic peak currents in proportional to the square root of scan rate (v). From these plots, one can notice that the current density and area under the CV curve increases with increasing scan rate indicating the fast diffusion of electrolyte ions on to the surface of the electrode surface. On the other hand, the capacitance of the hybrid films decreases with increasing scan rate (Figure 7b), which is due to the diffusion limit of electrolyte ions. Specific capacitance values of various graphene based $Ni(OH)_2$ composites are listed in Table S2 of the supporting information and the observed specific capacitance values of as synthesised hybrid films are comparable with the values reported in literature for similar materials.

Figure 8a displays the charge and discharge curves of bare $Ni(OH)_2$ and rGO–$Ni(OH)_2$ nanostructured hybrid films acquired

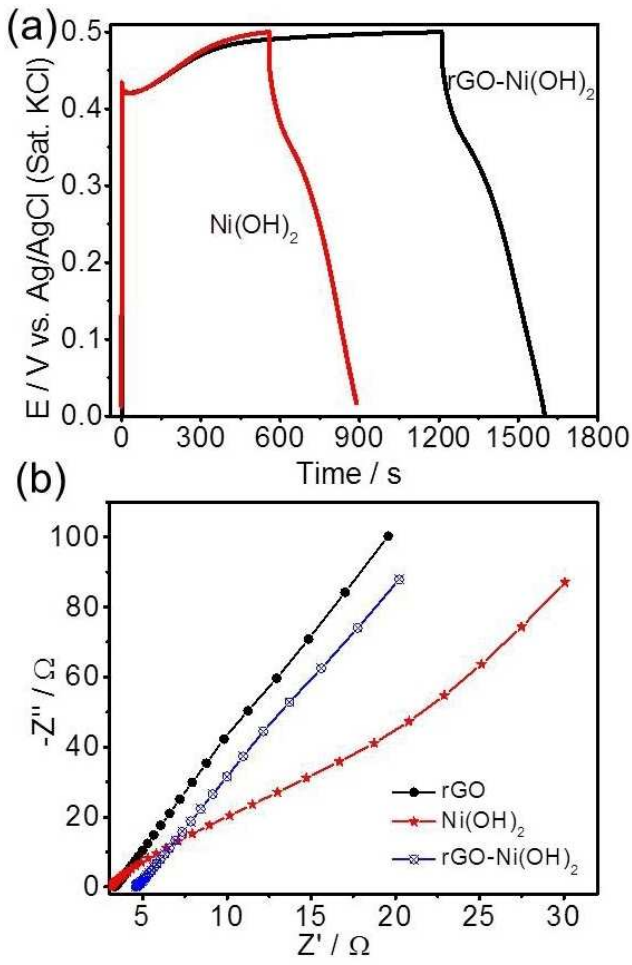

Figure 8. (a) Charge and discharge curves for bare $Ni(OH)_2$ and rGO–$Ni(OH)_2$ at 0.5 Ag^{-1} current density (b) Nyquist plots of various modified electrodes in 100 kHz to 0.01 Hz frequency range.

at a current density of 0.5 Ag^{-1}. The charge and discharge curves are not symmetrical and a small iR drop is observed in both the cases of films. The curves at various current densities such as 0.5, 1 and 2 Ag^{-1} are shown in Figure S9. It is well known that as the current density increases, the discharge time decreases and specific capacitance also decreases. The specific capacitance from the chronopotentiometry curves of these hybrid films has been calculated employing the following expression, $C_s = I_d t_d / Vm$, where I_d is the charge/discharge current, t_d is the time for a full discharge, V is the potential voltage window and m is the mass of the electrode material. The energy density and power density were calculated according to the expressions, $E = 0.5 C_s V^2$ and $P = E/t_d$, respectively.[22,23,63,29] At a current density of 0.5 Ag^{-1}, the energy density observed for rGO–$Ni(OH)_2$ nanostructured hybrid film ($E = 13.6$ Wh/kg) is higher than that of the bare $Ni(OH)_2$ film ($E = 11.4$ Wh/kg) with a power density of 125 W/kg. Figure 8b displays the Nyquist plots of various modified electrodes in the

frequency range, 100 kHz to 0.01 Hz. The plotsdisplay a semicircle at the higher frequency region and straight line at lower frequency region corresponding to electron transfer limited process and diffusion limited electron transfer process, respectively. rGO film modified electrode shows most ideal straight line along the imaginary axis implying that rGO acts as an ideal capacitor with fast ion diffusion process. The slope of the curves decreases in the following order rGO > rGO–$Ni(OH)_2$ > $Ni(OH)_2$ hybrid films indicating that the bare $Ni(OH)_2$ film exhibits a higher resistance towards electrolyte ion diffusion and as a result, lower capacitance.

We have also studied the cycle performance of rGO–$Ni(OH)_2$ supercapacitor electrode by measuring the specific capacitance from cyclic voltammetry at a scan rate of 100 mVs^{-1} for 10000 cycles (Figure 9). The hybrid film exhibits good

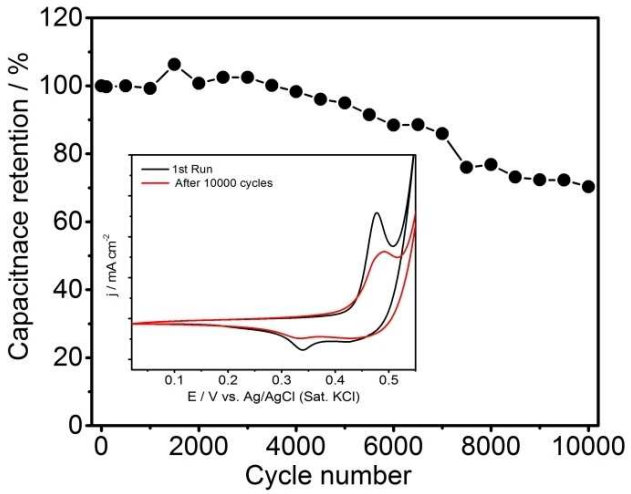

Figure 9. Specific capacitance retention vs. cycle number; inset shows the CV curves after 1st cycle and 10000 cycles for rGO–$Ni(OH)_2$ nanostructured hybrid film modified electrode.

stability even after 10000 cycles with a retention capacitance of 73%. The CVs acquired after 1st and 10000 cycles given in the inset show a slight reduction in redox peak after 10000 cycles. The superior electrochemical performance of the rGO–$Ni(OH)_2$ nanostructured hybrid film modified electrode can be attributed to the synergic effects of rGO and $Ni(OH)_2$. The rGO sheets prevent the aggregation of $Ni(OH)_2$ nanosheets during the cycling and aids in electron transport.

Conclusions

We have demonstrated energy generation and storage applications of free-standing, thin films of rGO–$Ni(OH)_2$ prepared by employing a facile and low-cost liquid/liquid interface method. The interface method involves a simple alkaline hydrolysis of the metal-organic precursor in the organic phase. The hybrid films are composed of highly ordered and interconnected Ni $(OH)_2$ sheets anchored on to rGO layers in a vertical fashion forming voids and the exquisite morphology of the films favours electrochemical applications. The hybrid film collected on steel substrate exhibits superior performance for OER and supercapacitor compared to that of bare $Ni(OH)_2$. An overpotential of 378 mV and 421 mV is required to achieve 10 mA cm^{-2} during OER for rGO–$Ni(OH)_2$ and bare $Ni(OH)_2$ with a Tafel slope of 56 mV dec^{-1} and 58 mV dec^{-1}, respectively, at par with RuO_2 and IrO_2 performance. The hybrid films also exhibit outstanding durability up to 1000 cycles and 40 hr with a very small increase in the overpotential. The nanowalls of Ni $(OH)_2$ over rGO also exhibit a high electrochemical surface area, 26.4 cm^2 and less charge transfer resistance, 2.8 Ω, compared to that of bare $Ni(OH)_2$ film. The estimated specific capacitance and areal capacitance of bare and hybrid films at 5 mVs^{-1} are 260 Fg^{-1} & 18.2 mF cm^{-2} and 1402 Fg^{-1} & 98.12 mF cm^{-2}, respectively. The presence of interconnected vertical walls of the catalyst with ordered voids permits maximum contact of the electrolyte with the active sites of the catalyst and rGO, rendering the films as ideal candidates for electrochemical applications. The rGO layers provide improved conductivity and also stability by hindering the aggregation of $Ni(OH)_2$ nanostructures during cycling. In view of the low-cost, facile and scalable preparation of the present electrodes, the liquid/liquid interface method may inspire the exploration of multifunctional nanostructured electrodes consisting of metal oxides, hydroxide and sulfides for diverse applications such as water splitting, supercapacitor, solar cells and fuel cells.

Supporting Information Summary

Experimental details, FESEM cross section images, AFM analysis, EDS mapping of hybrid films, and details of electrochemical measurements are provided in the Supporting Information.

Acknowledgements

The authors acknowledge funding from DST-Nanomission Thematic Project No. SR/NM/TP-25/2016.

Conflict of Interest

The authors declare no conflict of interest.

Keywords: Hybrid Films · $Ni(OH)_2$ Nanosheets · Oxygen Evolution Reactions · Reduced Graphene Oxide · Supercapacitors

[1] K. Zeng, D. Zhang, *Prog. Energy Combust. Sci.* **2010**, *36*, 307–326.
[2] M. Tahir, L. Pan, F. Idrees, X. Zhang, L. Wang, J.-J. Zou, Z. L. Wang, *Nano Energy* **2017**, *37*, 136–157.
[3] M. I. Jamesh, *J. Power Sources* **2016**, *333*, 213–236.
[4] Y. Lee, J. Suntivich, K. J. May, E. E. Perry, Y. Shao-Horn, *J. Phys. Chem. Lett.* **2012**, *3*, 399–404.
[5] H. B. Tao, L. Fang, J. Chen, H. Bin Yang, J. Gao, J. Miao, S. Chen, B. Liu, *J. Am. Chem. Soc.* **2016**, *138*, 9978–9985.
[6] K. Yan, G. Wu, W. Jin, *Energy Technol.* **2016**, *4*, 354–368.
[7] H. B. Tao, L. Fang, J. Chen, H. Bin Yang, J. Gao, J. Miao, S. Chen, B. Liu, *J. Am. Chem. Soc.* **2016**, *138*, 9978–9985.
[8] X. Li, D. Du, Y. Zhang, W. Xing, Q. Xue, Z. Yan, *J. Mater. Chem. A* **2017**, *5*, 15460–15485.

[9] J. M. Gonçalves, R. R. Guimaraes, C. V. Nunes, A. Duarte, B. B. N. S. Brandao, H. E. Toma, K. Araki, *RSC Adv.* **2016**, *6*, 102504–102512.
[10] G. Wang, L. Zhang, J. Zhang, *Chem. Soc. Rev.* **2012**, *41*, 797–828.
[11] Y. Liu, R. Wang, X. Yan, *Sci. Rep.* **2015**, *5*, 11095.
[12] A. Van der Ven, D. Morgan, Y. S. Meng, G. Ceder, *J. Electrochem. Soc.* **2016**, *153*, A210–A215.
[13] Z. Lu, Z. Chang, w. Zhu, X. Sun, *Chem. Commun.* **2011**, *47*, 9651–9653.
[14] S. Ruiz-Gómez, A. Boscá, L. Pérez, J. Pedros, J. Martinez, A. Páez, F. Calle, *Diamond Relat. Mater.* **2015**, *57*, 63–67.
[15] J. W. Lee, T. Ahn, D. Soundararajan, J. M. Ko, J.-D. Kim, *Chem. Commun.* **2011**, *47*, 6305–6307.
[16] H. Wang, H. S. Casalongue, Y. Liang, H. Dai, *J. Am. Chem. Soc.* **2010**, *132*, 7472–7477.
[17] S. Yang, X. Wu, C. Chen, H. Dong, W. Hu, X. Wang, *Chem. Commun.* **2012**, *48*, 2773–2775.
[18] X. Zhou, Z. Xia, Z. Zhang, Y. Ma, Y. Qu, *J. Mater. Chem. A* **2014**, *2*, 11799–11806.
[19] Y. Rao, Y. Wang, H. Ning, P. Li, M. Wu, *ACS Appl. Mater. Interfaces* **2016**, *8*, 33601–33607.
[20] J. Hao, K. Wu, C. Wan, Y. Tang, *Talanta* **2018**, *185*, 550–556.
[21] T. Gan, S. Hu, *Microchim. Acta* **2011**, *175*, 1.
[22] C. Wang, J. Xu, M.-F. Yuen, J. Zhang, Y. Li, X. Chen, W. Zhang, *Adv. Funct. Mater.* **2014**, *24*, 6372–6380.
[23] R. Wang, A. Jayakumar, C. Xu, J.-M. Lee, *ACS Sustain. Chem. Eng.* **2016**, *4*, 3736–3742.
[24] L. -A. Stern, X. Hu, *Faraday Discuss.* **2014**, *176*, 363–379.
[25] A. Harvey, X. He, I. J. Godwin, C. Backes, D. McAteer, N. C. Berner, N. McEvoy, A. Ferguson, A. Shmeliov, M. E. Lyons, V. Nicolosi, *J. Mater. Chem. A* **2016**, *4*, 11046–11059.
[26] H. Wu, T. Zhu, X. Lu, G. W. Ho, *J. Mater. Chem. A* **2017**, *5*, 24153–24158.
[27] O. Diaz-Morales, I. Ledezma-Yanez, M. T. Koper, F. Calle-Vallejo, *ACS Catal.* **2015**, *5*, 5380–5387.
[28] K. Bramhaiah, N. S. John, *RSC Adv.* **2013**, *3*, 7765–7773.
[29] K. Bramhaiah, I. Pandey, V. N. Singh, N. Kambhala, S. Angappane, N. S. John, *Mater. Chem. Phys.* **2018**, *209*, 1–9.
[30] K. Bramhaiah, N. S. John, *Adv. Nat. Sci. Nanosci. Nanotechnol.* **2012**, *3*, 045002.
[31] K. Bramhaiah, V. N. Singh, C. Kavitha, N. S. John, *J. Nanosci. Nanotechnol.* **2017**, *17*, 2711–2719.
[32] K. Bramhaiah, V. N. Singh, N. S. John, *Part. Part. Syst. Charact.* **2014**, *31*, 1168–1174.
[33] Q. Yang, Z. Lu, J. Liu, X. Lei, Z. Chang, L. Luo, X. Sun, *Prog. Nat. Sci.: Mater. Int.* **2013**, *23*, 351–366.
[34] L. Kumari, W. Z. Li, C. H. Vannoy, R. M. Leblanc, D. Z. Wang, *Cryst. Res. Technol.* **2009**, *44*, 495–499.
[35] H. Yan, D. Zhang, J. Xu, Y. Lu, Y. Liu, K. Qiu, Y. Zhang, Y. Luo, *Nanoscale Res. Lett.* **2014**, *9*, 424.
[36] N. Parveen, M. H. Cho, *Sci. Rep.* **2016**, *6*, 27318.
[37] D. S. Hall, D. J. Lockwood, C. Bock, B. R. MacDougall, *Proc. - R. Soc. Edinburgh, Sect. A: Math. Phys. Sci.* **2014**, *471*, 20140792.
[38] E. G. C. Neiva, M. M. Oliveira, M. F. Bergamini, L. H. Marcolino, A. J. G. Zarbin, *Sci. Rep.* **2016**, *6*, 33806.
[39] M. Hu, J. He, M. Yang, X. Hu, C. Yan, Z. Cheng, *RSC Adv.* **2015**, *5*, 26823–26831.
[40] W. Zhu, X. Yue, W. Zhang, S. Yu, Y. Zhang, J. Wang, J. Wang, *Chem. Commun.* **2016**, *52*, 1486–1489.
[41] J. L. Bantignies, S. Deabate, A. Righi, S. Rols, P. Hermet, J. L. Sauvajol and F. Henn, *J. Phys. Chem. C* **2008**, *112*, 2193–2201.
[42] P. Hosseini-Benhangi, M. A. Garcia-Contreras, A. Alfantazi, E. L. Gyenge, *J. Electrochem. Soc.* **2015**, *162*, F1356–F1366.
[43] Y. Dou, L. Zhang, J. Xu, C.-T. He, X. Xu, Z. Sun, T. Liao, B. Nagy, P. Liu, S. X. Dou, *ACS Nano.* **2018**, *12*, 1878–1886.
[44] Y. -H. Fang, Z.-P. Liu, *J. Am. Chem. Soc.* **2010**, *132*, 18214–18222.
[45] P. Tian, Y. Yu, X. Yin, X. Wang, *Nanoscale* **2018**, *10*, 5054–5059.
[46] Y. Li, C. Zhao, *Chem. Mater.* **2016**, *28*, 5659–5666.
[47] Z. Wu, Z. Zou, J. Huang, F. Gao, *J. Catal.* **2018**, *358*, 243–252.
[48] S. Klaus, y. Cai, M. W. Louie, L. Trotochaud, A. T. Bell, *J Phys. Chem. C* **2015**, *119*, 7243–7254.
[49] M. Gao, W. Sheng, Z. Zhuang, Q. Fang, S. Gu, J. Jiang, Y. Yan, *J. Am. Chem. Soc.* **2014**, *136*, 7077–7084.
[50] Y. Cheng, P. K. Shen, S. P. Jiang, *Int. J. Hydrogen Energy* **2014**, *39,* 20662–20670.
[51] X. Zhao, X. Ding, Y. Xia, X. Jiao, D. Chen, *ACS Appl. Nano Mater.* **2018**, *1*, 1476–1483.
[52] C. Tang, H. F. Wang, H. S. Wang, F. Wei, Q. Zhang, *J. Mater. Chem. A* **2016**, *4*, 3210–3216.
[53] D. Xiong, W. Li, L. Liu, *Chem. Asian J.* **2017**, *12*, 543–551.
[54] J. Ren, M. Antonietti, T. P. Fellinger, *Adv. Eng. Mater.* **2015**, *5*, 1401660.
[55] J. Jiang, A. Zhang, L. Li, L. Ai, *J. Power Sources* **2015**, *278*, 445–451.
[56] Z. Zhao, H. Wu, H. He, X. Xu, Y. Jin, *Adv. Funct. Mater.* **2014**, *24*, 4698–4705.
[57] H. Liang, F. Meng, M. Cabán-Acevedo, L. Li, A. Forticaux, L. Xiu, Z. Wang, S. Jin, *Nano Lett.* **2015**, *15*, 1421–1427.
[58] S. Niu, W. J. Jiang, T. Tang, Y. Zhang, J. H. Li, J. S. Hu, *Adv. Sci.* **2017**, *4*, 1700084.
[59] J. Nai, H. Yin, T. You, L. Zheng, J. Zhang, P. Wang, Z. Jin, Y. Tian, J. Liu, Z. Tang, L. Guo, *Adv. Eng. Mater.* **2015**, *5*, 1401880.
[60] S. Jung, C. C. McCrory, I. M. Ferrer, J. C. Peters, T. F. Jaramillo, *J. Mater. Chem. A,* **2016**, *4*, 3068–3076.
[61] L.-A. Stern, X. Hu, *Faraday Discuss.* **2014**, *176*, 363–379.
[62] C. C. L. McCrory, S. Jung, I. M. Ferrer, S. M. Chatman, J. C. Peters, T. F. Jaramillo, *J. Am. Chem. Soc.* **2015**,*137*, 4347–4357.
[63] F. Liu, X. Chu, H. Zhang, B. Zhang, H. Su, L. Jin, Z. Wang, H. Huang, W. Yang, *Electrochim. Acta.* **2018**, *269*, 102–110.

Submitted: October 25, 2018
Accepted: February 8, 2019